ACS APPLIED MATERIALS & INTERFACES

Research Article

www.acsami.org

# A Facile Route To Modify Ferrous Phosphate and Its Use as an Iron-Containing Resource for $LiFePO_4$ via a Polyol Process

Shaomin Li, Xichuan Liu, Rui Mi, Hao Liu,* Yinchuan Li, Woon-min Lau, and Jun Mei

Chengdu Development Center of Science and Technology, China Academy of Engineering Physics, Chengdu Green Energy and Green Manufacturing Technology Center, Chengdu, Sichuan Province 610207, China

Supporting Information

**ABSTRACT:** This study introduces an economical and environmentally friendly way of synthesizing $LiFePO_4/C$ to be used as cathode material in lithium ion batteries via two processes: (1) the synthesis of $LiFePO_4/C$ cathode material using a low cost divalent precursor ferrous phosphate, $Fe_3(PO_4)_2{\cdot}8H_2O$, as iron source in a polyol process and (2) the modification of the morphology of this precursor by varying the reaction time in a coprecipitation process. The study examines the effects of different structures and morphologies of the precursor on the structure and electrochemical performance of the as-synthesized $LiFePO_4/C$. The $LiFePO_4/C$ shows an excellent rate capability and cycle performance, with initial discharge capacities of 153, 128, and 106 mA h $g^{-1}$ at 1 C, 5 C, and 10 C. The capacity retention is respectively 98.7%, 98.2%, and 98.7%, after 10 cycles at the corresponding rates. The capacity retention remains at 97% even after 300 cycles at the rate of 10 C. The outstanding electrochemical performance can be attributed to the improved rate of $Li^+$ diffusion and the excellent crystallinity of synthesized $LiFePO_4/C$ powders through the modified precursor. Therefore, this is an economical and environmentally friendly way of synthesizing $LiFePO_4/C$ to be used as cathode material in lithium ion batteries.

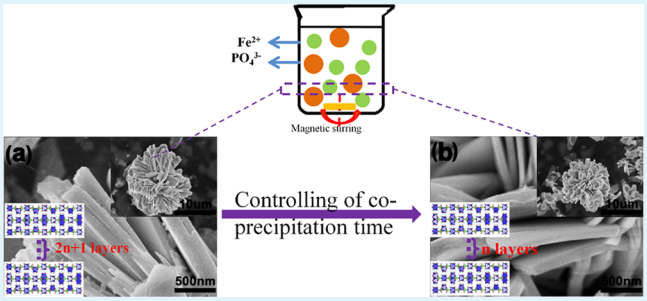


**KEYWORDS:** *$LiFePO_4/C$, ferrous phosphate, polyol, high rate, cyclability*

## 1. INTRODUCTION

So far, the lithium-ion battery is considered as one of the most promising technologies for the storage of electrical energy.[1] However, as power sources for high power equipment, such as electric vehicles, plug-in electric vehicles, and hybrid electric vehicles, as well as the utilization of intermittent renewable energies, its application is hindered by the high cost in production, safety concerns, and low energy and power density.[2] It is believed that these obstacles can at least be partly overcome if inexpensive and efficient cathode materials are developed. Among the many potential cathode materials, the $LiFePO_4$ (LFP) cathode has attracted great attention since its discovery in 1997,[3] owing to its numerous appealing merits, such as its environmental benignity, high thermal stability, relatively good cycle stability, and a flat discharge potential at 3.4 V vs $Li/Li^+$.[4−6] However, LFP's low electric conductivity ($\sim 10^{-11}$ S $cm^{-1}$) and low Li-ion diffusion dynamics ($\sim 1.8 \times 10^{-14}$ $cm^2$ $s^{-1}$) at room temperature,[5] which becomes even worse at lower temperatures,[7] restrict its application in fields that require high rate capability.

Many modifications have been tried to improve the rate performance of LFPs, such as dedicated controls of particle size,[8,9] shape, and morphology[10,11] to facilitate $Li^+$ diffusion, which preferably moves along the *b*-axis, and surface conductive coating[12,13] and ion doping[14,15] to enhance the migration of electrons. Usually two or more methods are combined together. Nevertheless, further research demonstrates that mass transport of $Li^+$ is more crucial for the improvement of the kinetics because its conductivity is several orders of magnitude lower than that of electrons along the three axes. In this regard, it appears that, rather than improving electron conductivity, facilitating Li ion diffusion, such as by shortening the [010] channels of LFP, might serve as a more promising solution to promote the rate performance of LFP.

Among the many present synthesis and structure control processes, some of them, such as the solid-state process,[16,17] coprecipitation in aqueous medium,[18,19] and the sol-gel route,[20,21] require a high temperature treatment, a procedure which leads to high energy consumption and, even worse, unwanted particle growth which causes detrimental impacts on lithium ion diffusion. Hence, low temperature techniques performed under hydrothermal or solvothermal conditions[22,23] have obvious superiority in this aspect because they offer good controllability in single phase formation, narrow particle size distribution in the range of nanoscale, and the capability of allowing the favorable (010) lattice plane to be exposed to the surface.[24] However, high pressure equipment and long reaction

Received: March 26, 2014
Accepted: May 26, 2014
Published: May 26, 2014

  

time are indispensible in these low temperature techniques, which would lead to high cost during synthesis.

In this regard, Prof. Kim et al. first reported the polyol process,[25] which is a modified solvothermal reaction under ambient pressure. With large (*ac*) facets exposed to the surface of the particle but no carbon layer coatings, the synthesized LFPs show an acceptable capacity of ∼50 mA h $g^{-1}$ at 60 C. Inspired by the satisfactory results, several studies follow with their focus on the effects of different polyol media on the crystal structure,[26] morphology,[27] and effects of varied kinds and contents of carbon resources on the electrochemical properties of carbon-coated LFP cathode material.[28,29] A comparison of the rate capacities of LFPs in these synthesis routes shows that divalent iron precursors could lead to relatively higher rate capabilities and cycle stabilities in the resultant LFPs compared with their trivalent iron counterparts.[24−28] However, the divalent iron precursors are more expensive than the trivalent ones. Besides, these studies still require a long reaction time (more than 10 h) at the boiling temperature of polyol medium, especially when water-soluble raw materials, such as iron acetate and ferric nitrate, are employed. To overcome these shortcomings, one needs to modify the polyol process to yield high performance LFP with less expensive divalent iron precursors in a reduced reaction time and to result in a product that should have a large (*ac*) facet with shorter [010] channel to facilitate a high rate capacity.

On the other hand, one of the divalent iron materials, ferrous(II) phosphate, ($Fe_3(PO_4)_2 \cdot 8H_2O$ ($F_3P_2$)), could be easily formed by aqueous precipitation from $FeSO_4$ in a few minutes and is therefore an inexpensive material to use. However, due to its quite small solubility products, it is not used as a reagent in the hydrothermal process for the synthesis of LFP. In his 2011 study, J. J. Chen argued that in a solvothermal process, the complete dissolution of the $F_3P_2$ required only ∼17 min and the formation of crystallite LFP was detected ∼5 min after the precursor began to dissolve,[30] which was indicative of a quicker polyol reaction. However, due to the rapid formation of $F_3P_2$, large particle size was obtained, which is an unfavorable morphological property.[24,31] Mechanical processes, such as ball-milling or aqueous sanding for hours, are generally utilized to reduce the particle size,[32] during which the abrasive materials could inevitably break off from the milling balls or sands, resulting in unwanted contaminations and extra energy expenses. Nevertheless, $F_3P_2$ might still be a good divalent iron precursor for the synthesis of LFP, if its particle size can be controlled by a nonmechanical process.

In this present work, we use the polyol process which allows for the LFP crystallization to take place in a mild environment. However, unlike other polyol processes using water-soluble or trivalent iron precursors, we use low cost ferrous phosphate. We control the crystal size of the precursor by systematically varying the reaction time instead of mechanical milling on the assumption that the growth rate is more or less time-dependent. We also systematically investigated the morphological effects of the precursor on the performance of the product (LFP). Using this modified polyol process and the optimized precursor, we have successfully reduced the reaction to within 5 h.

## 2. EXPERIMENTAL SECTION

**2.1. Materials.** Iron(II) sulfate heptahydrate ($FeSO_4 \cdot 7H_2O$, AR, 99.0%), ammonium phosphate monobasic ($NH_4H_2PO_4$, AR, 99.0%), ammonia solution (25.0%), phosphoric acid ($H_3PO_4$, AR, 85.0%), tri(ethylene glycol) (TEG, AR, 97.0%), and citric acid monohydrate ($C_6H_8O_7 \cdot H_2O$) were purchased from Chengdu Kelong Chemical reagent Co. (Chengdu, China). Lithium hydroxide monohydrate ($LiOH \cdot H_2O$, AR, 99.0%) was purchased from Sigma-Aldrich (Shanghai, China).

**2.2. Materials Preparation.** The $F_3P_2$ precursor was prepared through liquid coprecipitation under different controlled conditions, and the preparation procedures are described as follows.

$F_3P_2$: $NH_4H_2PO_4$ was added into a solution of $FeSO_4 \cdot 7H_2O$ at a molar ratio of 1:1 to obtain the embryo of $F_3P_2$. Then to the above suspension, which was still clear in appearance, $NH_3 \cdot H_2O$ was added drop by drop under vigorous stirring until the pH of the mixed solution was adjusted to 6.5. Stirring was continued for a few minutes until a blue-white suspension was formed. Finally the precursor was collected by filtration, washed several times with distilled water, and dried at 60 °C in a vacuum oven for 12 h. According to the different reaction time in the coprecipitation process, 5, 3, and 1 min, the samples of $F_3P_2$ were respectively named as I, II, and III.

LFP was synthesized by a polyol reduction process. $F_3P_2$, $H_3PO_4$, and proper amounts of $LiOH \cdot H_2O$ and citric acid were mixed in TEG (the molar ratio to iron is 10:1). The mixture was heated at 295 °C for 5 h in a round-bottom flask attached to a refluxing condenser equipped with a mechanical stirrer. To remove the TEG and other organic compounds, the resulting suspension was washed with acetone and alcohol and then centrifuged several times. To evaporate the remaining acetone and alcohol, the powder was dried in an airy place for 12 h. The synthesized powder obtained from $F_3P_2$ I, II, and III were denoted as $A_1$, $B_1$, and $C_1$. The LFP/C composites were obtained by heat treatment at 650 °C for 1 h under a flowing nitrogen atmosphere and were accordingly named as $A_2$, $B_2$, and $C_2$.

**2.3. Characterization.** The structure and phase purity of the $F_3P_2$, LFP, and LFP/C were characterized by X-ray diffraction (XRD, D/max 2200/PC, Rigaku, 40 kV, 20 mA, Cu $K_a$ radiation, $\lambda$ = 1.5406 Å). The size and morphology of the samples were observed with scanning electron microscopy (SEM, Hitachi S-5200) and field emission transmission electron microscopy (TEM, JEOL JEM-100CX). Fourier transformation infrared spectroscopy (FT-IR) was carried out on the samples using a Thermo IS10 FT-IR spectrometer. The chemical composition of the precursors was analyzed by X-ray photoelectron spectroscopy (XPS, Thermo Scientific ESCALAB 250XI). The thermal analysis was determined by a Mettler Toledo TG/DSC1 in air at a heating rate of 10 °C $min^{-1}$ from room temperature to 700 °C. The electrochemical properties were evaluated using CR 2032 cells consisting of the synthesized cathode, lithium metal as the reference electrode, and a Celgard 2500 separator. For the electrochemical measurements, the LFP/C materials, with a loading of 1−1.2 mg $cm^{-2}$, were mixed with 13 wt % carbon black and 7 wt % poly(tetrafluoroethylene) binder (purchased from Sinopharm Chemical Reagent Co.). This mixture was coated on an aluminum mesh and dried under vacuum at 100 °C for 12 h before cell assembly. The electrolyte used was a 1:1 (in volume) mixture of ethylene carbonate (EC) and dimethyl carbonates (DMC) containing 1 M $LiPF_6$, purchased from Zhangjiagang Guotai-Huangrong New Chemical Materials Co., Ltd. The galvanostatic charge and discharge were controlled between 2.5 and 4.3 V on an Arbin BT2000 instrument. Electrochemical impedance spectroscopy (EIS) measurements were carried out in two-electrode cells on a CHI-660D electrochemistry workstation, using a ±5 mV AC signal amplitude and frequency range from 0.1 to 100 kHz, and cycling voltametry (CV) results were obtained in the range of 2.5 to 4.3 V by the same station.

## 3. RESULTS AND DISCUSSION

The SEM images of three kinds of $F_3P_2$ precursors are depicted in Figure 1. As shown, precursor I and II tend to crystallize layer by layer. These layers are arranged in alternating and overlapping planes, spreading out radially as a flower corolla. This is because it is easier for $F_3P_2$ to form a three-dimensional framework by connecting a single or dimeric ($FeO_6$) octahedral groups with one ($PO_4$) tetrahedral group in the *ac* plane, and

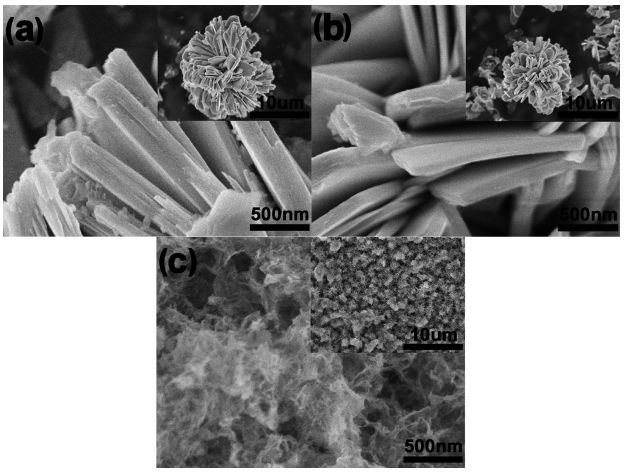


**Figure 1.** SEM images of $F_3P_2$ precursors I (a), II (b), and III (c). Insets are low magnification images.

the repetition of these planes make up an infinite layer parallel to the *ac* face by an intricate network of hydrogen bonds,[33] as illustrated in Figure 2. However, different from I and II,

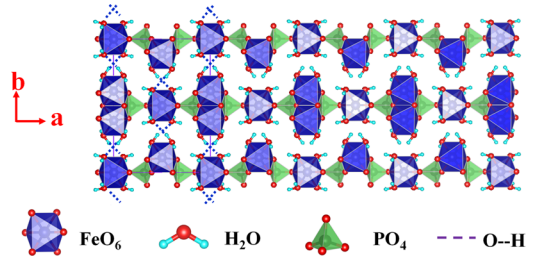


**Figure 2.** Illustration for the crystal structure of the precursor.

precursor III presents a continuous network of laminated layers which is assumed to act as nuclei in the precipitates. As the reaction is prolonged, adjacent nuclei have sufficient time to join together at a planar interface and to crystallize down *b* axis as shown in Figure 1a,b. From the images, we can tell that the morphology of the precursor can be controlled by varying the reaction time in the coprecipitation process as we assumed. The XRD patterns of $F_3P_2$ precursors obtained under different reaction times are shown in Figure 3a.

All the peaks of precursors I and II are indexed as a monoclinic structure with a space group of $I_{2/m}$ (12) (JCPDS card no.: 30-0662). The patterns also show that with increasing reaction time in the coprecipitation process, the ratio of the intensity of (020) to (200) significantly increases, as $F_3P_2$ forms infinitely many layers by stacking $PO_4$−$FeO_6$ monolayers via the O−H···H hydrogen bond along the *b* axis, making a three-dimensional framework,[34] an observation which confirms our previous suggestion that the layer structure observed with SEM is attributed to the conjunction of $PO_4$ and $FeO_6$ groups. Moreover, $F_3P_2$ III with reaction time of 1 min shows an amorphous structure with broad peaks exhibited around standard peaks, which is presented as laminated layers in the SEM images of Figure 1c mentioned above.

The IR spectra of the three precursors are depicted in Figure 3b. According to previous studies, one can interpret these spectra on the basis of characteristic vibrations of water hydroxyl stretching, water HOH bending, and PO stretching.[35] As for $F_3P_2$ I and II, one can describe the water OH stretching broad band as the convolution of two bands at around 3469 and 3269 $cm^{-1}$, values which are in good agreement with the literature.[36] The observation also indicates that it is this hydrogen bonding which holds adjacent sheets together. Water HOH bending modes region ($\upsilon_2$ symmetric bending mode) occurs at around 1634 $cm^{-1}$, indicating coordinated water and chemically bonded water. Several bands around 1630 $cm^{-1}$ are observed, which should originate from water at different sites in the precursor structure. In the unit cell of ferrous phosphate, there are two formula units ($F_3P_2{\cdot}8H_2O$) per unit cell. Since $Z$ = 2, it means that there are 16 water molecules in one unit cell. The bands at 809 $cm^{-1}$ are due to water libration modes of strongly hydrogen bonded water molecules. In addition, the most intense IR bands for phosphates are observed around 1047 $cm^{-1}$ and are assigned to the antisymmetric stretching vibration. Other frequencies observed below 1000 $cm^{-1}$ can be assigned to the $\upsilon_1$ and $\upsilon_4$ modes of the $PO_4$ group.[37] However, the spectral data of $F_3P_2$III is at variance with those of I and II, displaying a red shift to 3390 $cm^{-1}$ and is weak or of zero absorbance around 809 $cm^{-1}$. Because $F_3P_2$ crystal packing can be described as a layered structure with parallel *ac* faces by an intricate network of H-bonds between layers, the changed bands in III ought to result from the variation of hydrogen stretching, which probably suggests the diminution of the water OH stretching mode of interlayers due to the reduced amount of bonds. The protons of water molecules in outer planes may not bind with other $H_2O$ groups and thus impair the interlayer

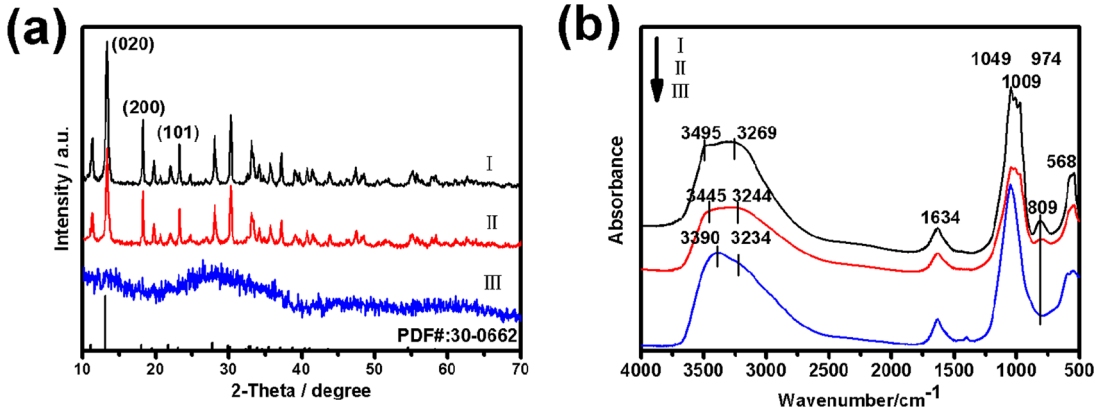


**Figure 3.** XRD patterns (a) and infrared spectra (b) of the $F_3P_2$ precursors obtained by coprecipitation for different reaction times.


dx.doi.org/10.1021/am501762x | ACS Appl. Mater. Interfaces 2014, 6, 9449−9457

interaction, an outcome which assures the tying of the same layers within the three-dimensional framework.

XPS is employed to characterize the composition and the oxidation state of iron in each precursor. Three precursors exhibit three main peaks identified in the XPS spectra, corresponding to Fe 2p, O 1s, P 2s, and P 2p, as shown in Figure S1a, Supporting Information.[38]The Fe 2p spectra for the precursors are deconvoluted into two components in Figure S1b–d, Supporting Information. The peaks at around 710.8 and 723.8 eV can be ascribed to the presence of $Fe^{2+}$ in the precursors. Peaks at around 713.5 and 727.4 eV are related to $Fe^{3+}$ which result from the oxidation of ferrous phosphate suspension when exposed to air during the filtration process. In addition, the $Fe^{2+}$ $2p_{3/2}$ peaks exhibit an asymmetric tail to higher binding energy ascribed to the surface structures, a phenomenon which is common in other iron-containing compounds.[39]The contents of ferrous species are observed to decrease with the increasing time in coprecipitation, as the ratio of $Fe^{2+}$/ $Fe^{3+}$ is 1.92, 2.05, and 2.16 for precursors I, II and III. As confirmed by various characterizations, the crystal structure and morphology of the precursor are controlled successfully by varying the coprecipitation time.

The size and morphology of LFP/C powders obtained from the different precursors, with and without heat treatment, are shown in Figure 4. After 5 h of refluxing, the morphologies of

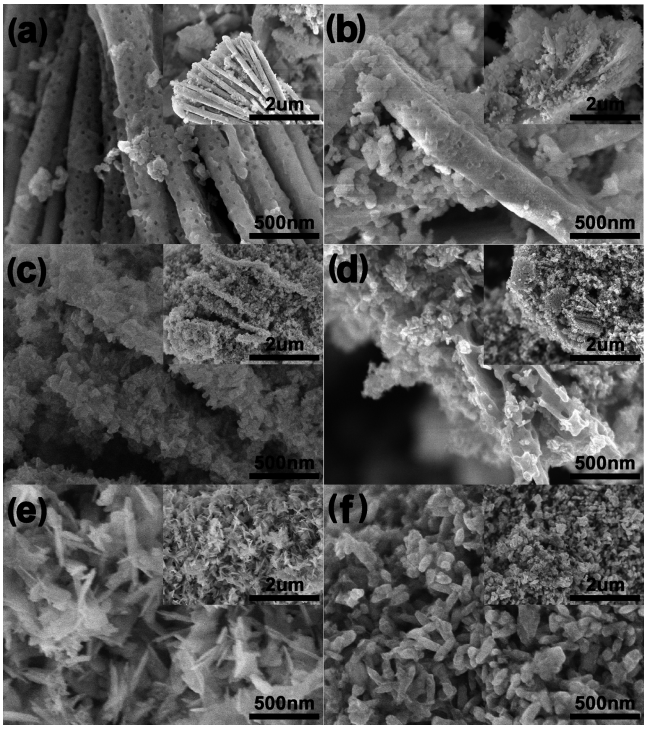


**Figure 4.** SEM images of $A_1$ (a), $B_1$ (c), and $C_1$ (e) samples after 5 h of refluxing using different precursors. The corresponding samples $A_2$ (b), $B_2$ (d), and $C_2$ (f) with post treatment for 1 h.

samples $A_1$, $B_1$, and $C_1$ became quite different. Two phases of platelike structure and small particles on the plate surfaces are both presented in sample $A_1$, while in $B_1$, more contents of particles are shown compared with that in A1, which is also detected in the solvothermal method.[40] In comparison, large platelike structure in $C_1$ disappears. This difference can be attributed to the varied crystal size of the precursor. Classical nucleation theory argues that smaller particles dissolve and larger particles grow by adsorbing monomers from the dissolved particles.[41] In this case, the weak bonded sites of precursor III might dissolve prior to the strong ones. Then the surface of strong bonded sites would adsorb active monomers driven by surface energy minimization, allowing continuous growth until a pseudoequilibrium state is reached.

After heat treatment, more nanoparticles develop in $A_2$ and $B_2$ but layered precursors remained, demonstrating that during the 1 h pyrolysis conversion, the overall particle morphology is preserved to some extent. Nevertheless, $C_2$ shows rodlike particles of homogeneous distribution, about 160 nm in length and 80 nm in width, with less agglomeration and better dispersion than that of samples $A_2$ and $B_2$, as observed from Figure 4. It is believed that the small particle size of $F_3P_2$ contributes to the formation of nanopowders with monodispersity, which is also demonstrated in other research.[32]

The XRD patterns of the as-prepared powders before heat treatment are shown in Figure 5a. The main diffraction peaks of these powders are indexed on the basis of an orthorhombic structure with space group of $P_{nma}$ (62), demonstrating that the growth of LFP can be achieved in the polyol process using the precursor of $F_3P_2$ in less than 5 h as J. J. Chen reported.[30] However, in sample $A_1$, an obvious amorphous feature around 20–40° demonstrated a low degree of crystallinity, and impurities of $F_3P_2$ were also detected at 11.1° and 13.1°, which can be indexed to the (110) and (020) faces of precursor, respectively.

In addition, different from sample $A_1$, $C_1$ exhibits higher crystallization, indicating that the modified morphology of precursor III facilitates the formation of high crystalline LFP powders, which is probably due to the lower potential dissolution barriers of laminated layers, and thus $F_3P_2$ III tends to dissolve in the polyol process more easily than its thicker counterparts.

Figure 5b demonstrates that all the diffraction peaks of the samples after heat treatment are perfectly indexed to the orthorhombic olivine structure with the exception of sample $A_2$, which shows obvious impurities at 13.1°. The strongest diffraction peak of (020) faces of precursor $F_3P_2$ is shown in Figure 3a. Here, no diffraction peaks of carbon are identified, suggesting that carbon yielded from the decomposition of citric acid exists as an amorphous phase. Sample $C_2$ produced from $F_3P_2$ III exhibits a crystallinity higher than that of samples $A_2$ and $B_2$, while all of them have refined cell parameters in agreement with those of the stoichiometric bulk phase ($a$ = 10.332, $b$ = 6.01, $c$ = 4.692 nm, JCPDS card no.: 81-1173).[25] Clearly, the $F_3P_2$ precursors of small particle size and weakened *ac* plane packing promote the dissolution in polyol and the formation of highly crystallized olivine phase while residual contents of $F_3P_2$ precursor are accordingly reduced. As electrochemical lithium intercalation and deintercalation are, in general, limited by the rate of diffusion,[42] the particle size of cathode materials is an important factor that determines the electrochemical performance. Small particle size shortens the diffusion pathway and increases the contact area between the electrode and the electrolyte. Therefore, sample $C_2$ is assumed to deliver a better electrochemical performance.

Figure 6a shows the initial charge/discharge profiles of the LFP/C composites, i.e., $A_2$, $B_2$, and $C_2$ tested in the range of 2.5 to 4.3 V at 0.1 C rate. Three samples exhibit the typical flat voltage plateau between 3.5 and 3.4 V (vs. $Li/Li^+$), an observation that is attributed to the $Fe^{2+}/Fe^{3+}$ redox couple during lithium-ion extraction and insertion processes.[3]

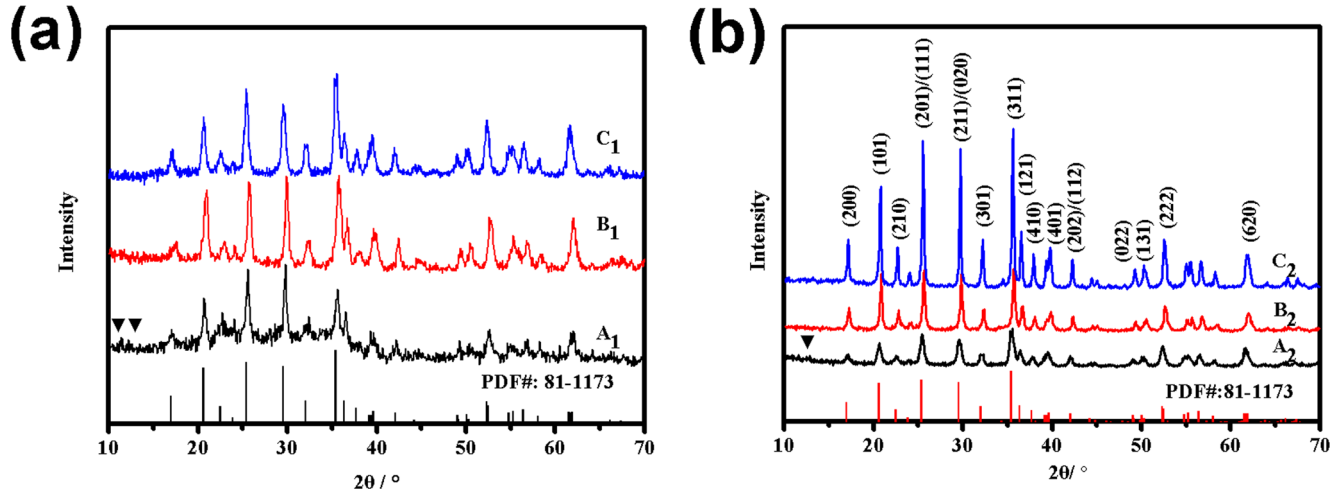


**Figure 5.** XRD patterns of samples before (a) and after (b) heat treatment. Impurities indicated by the symbol ▼.

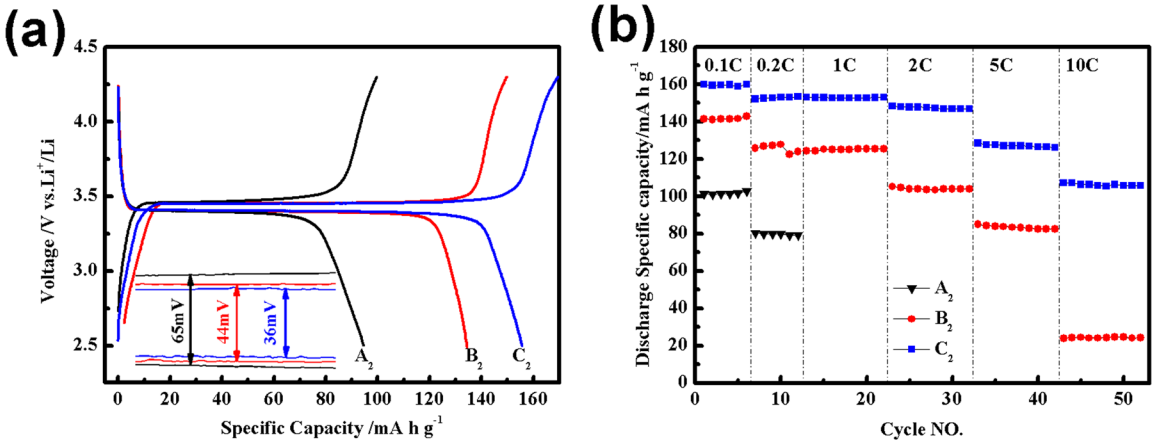


**Figure 6.** (a) Charge/discharge profiles of three samples at first cycle at 0.1 C, (b) the cyclability and rate capability of three samples at various discharge rates from 0.1 to 10 C.

Generally, the initial charge plateau is wider than the discharge one in all three samples, which results from adding excess contents of lithium salt in the polyol reduction process, a process corresponding to more lithium ions being extracted from the LFP/C crystal structure during the first charge. As shown in Figure 6a, sample $C_2$ delivers the highest discharge capacity of 158 mA h $g^{-1}$, compared to 103 and 140 mA h $g^{-1}$ for $A_2$ and $B_2$, respectively. Additionally, the voltage difference between the charge/discharge plateau of $C_2$ is smaller than that in the other electrodes (65, 44, and 36 mV for $A_2$, $B_2$, and $C_2$, respectively), indicating the superior electrochemical kinetics for the former, which should be ascribed to the single phase composition and more uniform particle size distribution.[42]

Figure 6b is the contrast discharge curves at various rates (0.1 C to 10 C). With an increase of the discharge current density, capacities generally decrease, a phenomenon which is also detected in many other studies and is shown to be a result of the increase of the internal resistance at high C-rate where thermodynamic equilibrium cannot be reached.[42] As expected, $C_2$ has a better rate performance, presenting the capacities of 158, 154, 153, 148, 128, and 106 mA h $g^{-1}$ at 0.1, 0.2, 1, 2, 5, and 10 C. However, in $A_2$ and $B_2$, a small quantity of precursors is not converted to LFP and becomes severely agglomerated, which is not beneficial for the immersion of the electrolyte.

EIS is used to further analyze the electrode impedance of three samples $A_2$, $B_2$, and $C_2$. As shown in Figure S2, Supporting Information, the semicircle in the high-frequency region represents charge transfer resistance. The straight line in the low-frequency region is ascribed to the diffusion of the lithium ions into the bulk of electrode material. The equivalent electrical circuit model is illustrated as an inset. The impedance spectra can be explained with uncompensated resistance ($R_e$), charge-transfer resistance ($R_{ct}$), double layer capacitance and passivation film capacitance (CPE), and Warburg impedance ($Z_\omega$). The fitting values from this equivalent circuit are presented in Table S1, Supporting Information. It shows a much smaller depressed semicircle in $B_2$ and $C_2$ electrodes compared to $A_2$. Thus, the charge transfer resistance of $B_2$ and $C_2$ may be much smaller than that of $A_2$ composite, resulting in a higher electronic conductivity of $B_2$ and $C_2$. In addition, the lithium-ion diffusion coefficient can be calculated according to the following equation:[43]

$$D = 0.5R^2T^2A^{-2}n^{-4}F^{-4}C^{-2}\sigma_\omega{}^{-2}$$

$R$ is the gas constant, $T$ is the absolute temperature, $A$ is the surface area of the cathode, $n$ is the number of electrons per molecule during oxidization, $F$ is the Faraday constant, $C$ is the molar concentration of lithium ion (moles per cubic


dx.doi.org/10.1021/am501762x | ACS Appl. Mater. Interfaces 2014, 6, 9449−9457

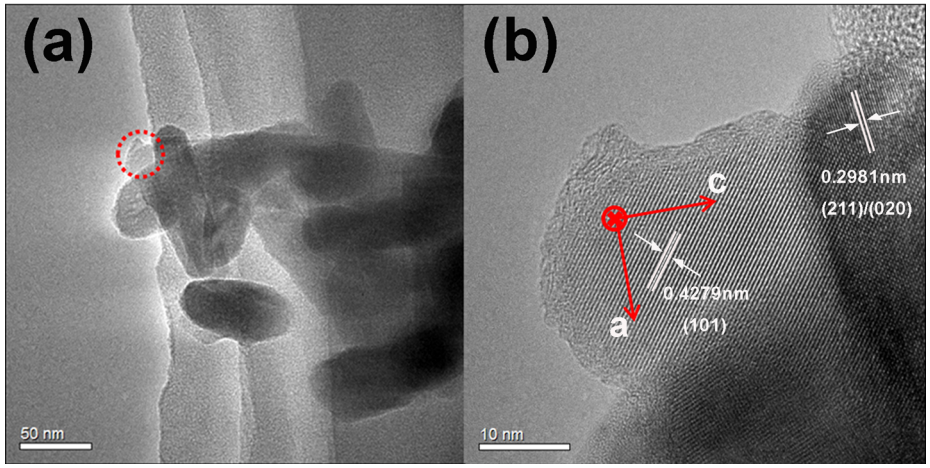


**Figure 7.** HR-TEM image of synthesized LFP/C (a) and a high resolution view of the inside circled area in panel a (b).

centimeter), and $\sigma_\omega$ is the Warburg factor which is relative to $Z'$:

$$Z' = \mathrm{Re} + R_{ct} + \sigma_\omega^{-1/2}$$

Figure S2b, Supporting Information, shows the relationship between $Z'$ and square root of frequency ($\omega^{-1/2}$) in the low frequency region. A linear characteristic could be seen in both curves. The diffusion coefficient of lithium ion of $A_2$, $B_2$, and $C_2$ are $2.03 \times 10^{-14}$, $2.13 \times 10^{-13}$, and $2.48 \times 10^{-13}$ $cm^2$ $s^{-1}$, respectively. As shown in Figure 5b, the diffusion coefficient of lithium ion in $B_2$ and $C_2$ is 1 order greater than that of $A_2$, which can be attributed to the higher crystallinity property in $B_2$ and $C_2$ than in $A_2$. Apparently, $C_2$ possesses the smallest $R_{ct}$ and highest lithium-ion diffusion coefficient $D_{Li}^+$ among all the samples. This EIS characterization explains well why $C_2$ presents the highest discharge specific capacity at various discharge rates.

Figure 7a,b shows the HRTEM images in low and high magnification, respectively, of $C_2$. It is apparent that the LFP/C particles prepared by the polyol process exhibit high crystallinity, which plays an important role in the electrochemical stability of the electrode material.[44] The interplanar distance is estimated to be 4.279 Å, which is in good agreement with the (101) planes of the olivine LFP. This beneficial structure may be due to the prior adsorption of organic solvent on the {010} faces of LFP which in turn yield a kinetic control of growth rates of the facets, leading to the improvement of lithium-ion diffusion coefficient as Table 1S, Supporting Information, shows.[45] In addition, the carbon layer yielded from 650 °C treatment can be evenly coated, as thin as ~2.6 nm for isolated particles. The carbon content of $C_2$ is about 4 wt %, measured by the TG analysis as shown in Figure S3, Supporting Information.[10]

The uniform carbon coating on the surface of LFP might originate from a polyester network, which is induced by esterification reaction between citric acid and TEG and then transformed into the uniform carbon layer after high temperature calcinations. A similar process occurs between citric and ethylene glycol as Ma[46] found. This thin and even coating allows lithium ions to easily intercalate into the framework of LFP.[47]

Results of further charge/discharge tests at high rates are shown in Figure 8, confirming the outstanding cyclability and rate capability of sample $C_2$, which shows 97.6% and 81.5%

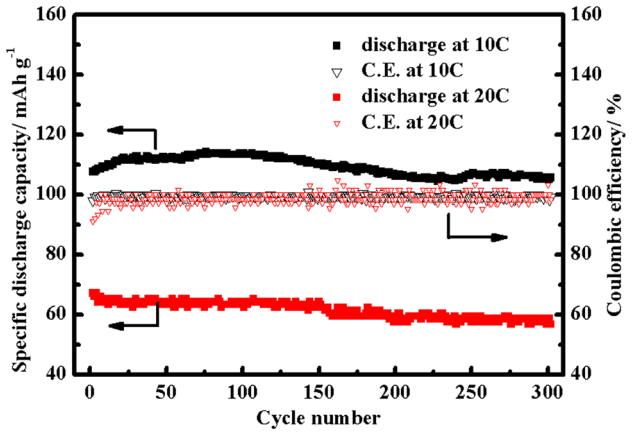


**Figure 8.** Rate capability of LFP/C sample $C_2$ at the discharge rates of 10 and 20 C.

capacity retention at 10 and 20 C after 300 cycles, along with a steady coulombic efficiency around 100% at every cycle. The increased discharge capacity around 50 cycles at 10 C could be ascribed to more complete infiltration of electrolyte into electrode material and the increased internal temperature caused by high charge/discharge rate. The excellent electrochemical properties benefit from the high crystallization, narrow particle size distribution, uniform carbon coating,[48] and more importantly, the large (*ac*) facets exposed to the surface of the particle. Similar cycle stabilities at lower rates are also observed in Figure S4, Supporting Information.

To provide more information on the improved electrochemical properties of $C_2$, the cyclic voltammetry tests were carried out at a scan rate of 0.1 mV $s^{-1}$, as shown in Figure 9a. The CV shows sharp and symmetric anodic/cathodic peaks, located at about 3.51 and 3.35 V vs $Li/Li^+$ reference electrode, which corresponds to the $Fe^{2+}/Fe^{3+}$ redox reaction during the intercalation/deintercalation process. No virtual changes are observed on the amplitude and shape of the redox peaks after three cycles. This indicates the good stability of lithium intercalation/deintercalation reactions in LFP/C sample $C_2$ as has also been demonstrated in the charge/discharge profiles. Figure 9b shows the CVs of sample $C_2$ synthesized from $F_3P_2$ III at different scan rates, ranging from 0.1 to 5.0 mV $s^{-1}$, during which paired peaks represent the typical two-phase electrochemical reaction. A plot of peak current density with

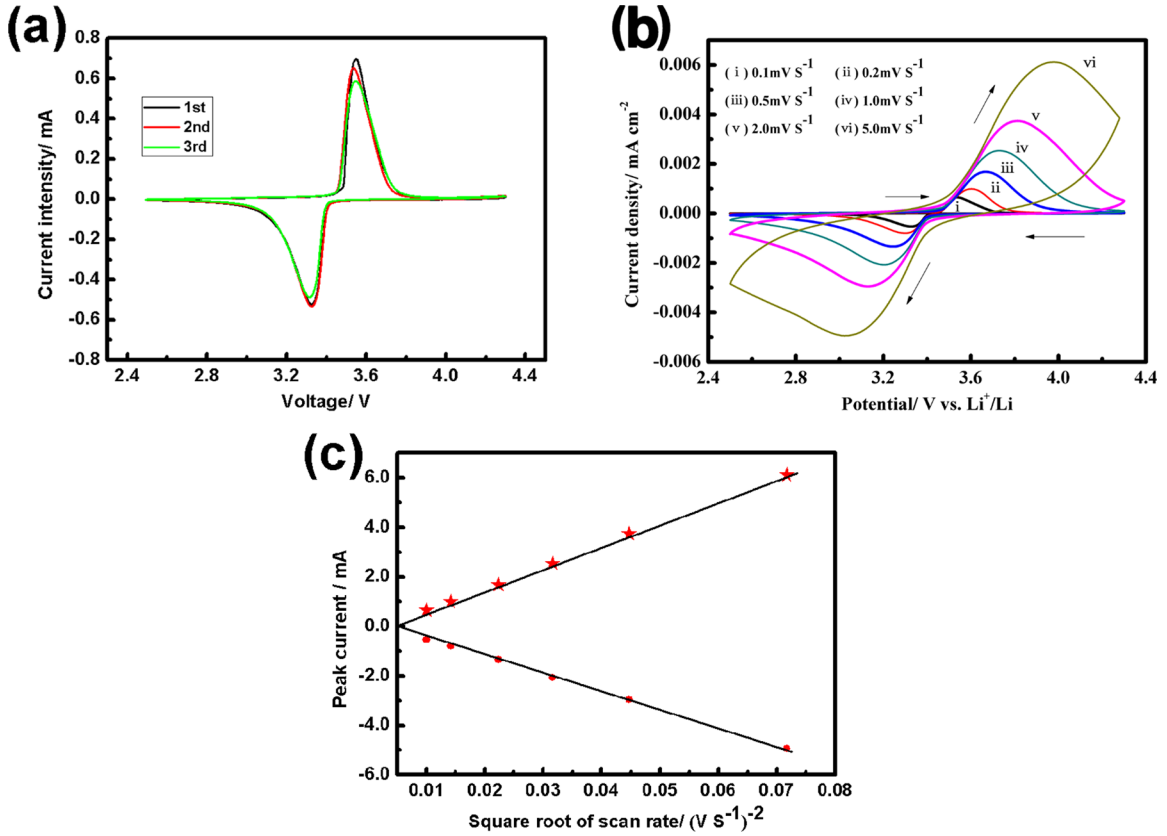


**Figure 9.** (a) Cyclic voltammetry (CV) profiles of LFP/C composites synthesized at a scan rate of 0.1 mV $s^{-1}$, (b) CVs of LFP/C composites at different scan rates, and (c) plot of peak current vs square root of scan rate.

the square root of the scan rate is shown in Figure 9c. The linear dependence of current with the square root of the scan rate suggests that the reversible reaction is a diffusion-control process. Thus, the rodlike LFP/C composites exhibit high electrochemical activity.

## 4. CONCLUSION

LFP/C composites have been synthesized from a low-cost divalent Fe-containing precursor in a polyol process in a relative short reaction time. The optimum electrochemical capacities of these LFP/C composites are 153, 128, 106, and 70 mA h $g^{-1}$ at 1, 5, 10, and 20 C discharge rates, respectively, with excellent capacity retention even after 300 cycles. The high rate performance is attributed to the uniform particle size distribution in the range of 100−200 nm and the large *ac* facets exposed to the surface of the particle. We have demonstrated that such morphology can be modified by systematic control of the particle size and shape of the $Fe_3(PO_4)_2{\cdot}8H_2O$ precursor. Decreasing the thickness of precursor down its *b* axis improves the rate capacities of the LFP/C samples.

## ■ ASSOCIATED CONTENT

### Supporting Information

Figure S1 shows the XPS spectrum of the three precursors. Figure S2 gives the Nyquist plots of three LFP/C samples and the relationship plot between $Z'$ and $\omega^{-1/2}$ in the low-frequency region. TG and DTA curves of the LFP/C sample $C_2$ are shown in Figure S3. Figure S4 presents cycle stability of $C_2$ at low current densities. Kinetic parameters of different LFP/C samples are shown in Table S1. This material is available free of charge via the Internet at http://pubs.acs.org.

## ■ AUTHOR INFORMATION

### Corresponding Author

*Tel: 0086-28-67076208. E-mail: mliuhao@gmail.com.

### Notes

The authors declare no competing financial interest.

## ■ ACKNOWLEDGMENTS

The authors appreciate the financial support from Science & Technology Department of Sichuan Province (2013GZX0145-3). We are indebted to Margaret Yau, Jiahui Lin, and Yong Jin for their kind help and fruitful discussions.

## ■ REFERENCES

(1) Wang, Y.; Cao, G. Z. Development in Nanostructured Cathode Materials for High-Performance Lithium-Ion Batteries. *Adv. Mater.* **2008**, *20*, 2251−2269.

(2) Amjad, S.; Neelakrishnan, S.; Rudramoorthy, R. Review of Design Considerations and Technological Challenges for Successful Development and Deployment of Plug-in Hybrid Electric Vehicles. *Renewable Sustainable Energy Rev.* **2010**, *14*, 1104−1110.

(3) Padhi, A. K.; Nanjundaswamy, K. S.; Goodenough, J. B. Phospho-Olivines as Positive-Electrode Material for Rechargeable Lithium Batteries. *J. Electrochem. Soc.* **1997**, *4*, 1188−1194.

(4) Sundarayya, Y.; Kumaraswamy, K.C.; Sunandana, C. S. Sudden Olivine $LiFePO_4$ Nanocrystallisation by Progressive Introduction of Li into Ferrous Phosphate Structure. *Mater. Res. Soc. Symp. Proc.* **2007**, 1023.

(5) Lou, X. M.; Zhang, Y. X. Synthesis of $LiFePO_4$/C Cathode Materials with Both High-Rate Capacity and High Tap Density for Lithium-Ion Batteries. *J. Mater. Chem.* **2011**, *21*, 4156−4160.
(6) Miranda, Á.G.; Hong, C.W. Integrated Modeling for the Cyclic Behavior of High Power Li-Ion Batteries under Extended Operating Conditions. *Appl. Energy* **2013**, *111*, 681−689.
(7) Zheng, J. C.; Zhang, B.; Zhang, M.; Wu, L. Low-Temperature Electrochemical Performance of $LiFePO_4$/C Cathode with 3D Conducting Networks. *Chem. Lett.* **2012**, *41*, 232−233.
(8) Yamada, A.; Chung, S. C.; Hinokuma, K. Optimized $LiFePO_4$ for Lithium Battery Cathodes. *J. Electrochem. Soc.* **2001**, *148*, A224−A229.
(9) Xie, M.; Zhang, X. X.; Laakso, J.; Wang, H.; Levänen, E. New Method of Postmodifying the Particle Size and Morphology of $LiFePO_4$ via Supercritical Carbon Dioxide. *Cryst. Growth Des.* **2012**, *12*, 2166−2168.
(10) Kong, L. B.; Zhang, P.; Liu, M. C.; Liu, H.; Luo, Y. C.; Kong, L. Fabircation of Promising $LiFePO_4$/C Composite with a Core−Shell Structure by a Moderate in Situ Carbothermal Reduction Method. *Electrochim. Acta* **2012**, *70*, 19−24.
(11) Lee, M. H.; Kim, J. Y.; Song, H. K. A Hollow Sphere Secondary Structure of $LiFePO_4$ Nanoparticles. *Chem. Commun.* **2010**, *46*, 6795−6797.
(12) Yang, J. L.; Wang, J. J.; Tang, Y. J.; Wang, D. N.; Xiao, B. W.; Li, X. F.; Li, R. Y.; Liang, G. X.; Sham, T. K.; Sun, X. L. In Situ Self-Catalyzed Formation of Core−Shell $LiFePO_4$@CNT Nanowires for High Rate Performance Lithium-Ion Batteries. *J. Mater. Chem. A* **2013**, *1*, 7306−7311.
(13) Jiang, Q.; Xu, Y. L.; Zhao, C. J.; Qian, X. Z.; Zheng, S. W. $LiFePO_4$/CA Cathode Nanocomposite with 3D Conductive Network Structure for Li-Ion Battery. *J. Solid State Electrochem.* **2012**, *16*, 1503−1508.
(14) Shu, H. B.; Wang, X. Y.; Wu, Q.; Hu, B. N.; Yang, X. K.; Wei, Q. L.; Liang, Q. Q.; Bai, Y. S.; Zhou, M.; Wu, C.; Chen, M. F.; Wang, A. W.; Jiang, L. L. Improved Electrochemical Performance of $LiFePO_4$/C Cathode via Ni and Mn Co-Doping for Lithium-Ion Batteries. *J. Power Sources* **2013**, *237*, 149−155.
(15) Sun, C. S.; Zhang, Y.; Zhang, X. J.; Zhou, Z. Structural and Electrochemical Properties of Cl-Doped $LiFePO_4$/C. *J. Power Sources* **2010**, *195*, 3680−3683.
(16) Lai, C. Y.; Xu, Q. J.; Ge, H. H.; Zhou, G. D.; Xie, J.Y. Improved Electrochemical Performance of $LiFePO_4$/C for Lithium-Ion Batteries with Two Kinds of Carbon Sources. *Solid State Ionics* **2008**, *179*, 1736−1739.
(17) Pan, M. S.; Zhou, Z. T. Carbon Rich Surface of $LiFePO_4$ Grain Enhancing Its Rate Capability. *Mater. Lett.* **2011**, *65*, 1131−1133.
(18) Park, K. S.; Kang, K. T.; Lee, S. B.; Kim, G. Y.; Park, Y. J.; Kim, H. G. Synthesis of $LiFePO_4$ with Fine Particle by Co-Precipitation Method. *Mater. Res. Bull.* **2004**, *39*, 1803−1810.
(19) Lv, Y.; Wang, L. X.; Lu, D.; Sun, J.; Sun, J. C. Synthesis of $LiFePO_4$ by Co-Precipitation and Optimization of Its Performance. *Key Eng. Mater.* **2012**, *519*, 132−136.
(20) Ma, J.; Li, B. H.; Du, H. D.; Xu, C. J.; Kang, F. Y. Inorganic-Based Sol−Gel Synthesis of Nano-Structured $LiFePO_4$/C Composite Materials for Lithium Ion Batteries. *J. Solid State Electrochem.* **2012**, *16*, 1353−1362.
(21) Lin, Y.; Wu, J. B.; Chen, W. P. Enhanced Electrochemical Performance of $LiFePO_4$/C Prepared by Sol−Gel Synthesis with Dry Ball-Milling. *Ionics* **2013**, *19*, 227−234.
(22) Brochu, F.; Guerfi, A.; Trottier, J.; Kopeć, M.; Mauger, A.; Groult, H.; Julien, C. M.; Zaghib, K. Structure and Electrochemistry of Scaling Nano C-$LiFePO_4$ Synthesized by Hydrothermal Route: Complexing Agent Effect. *J. Power Sources* **2012**, *214*, 1−6.
(23) Devaraju, M. K.; Honma, I. Hydrothermal and Solvothermal Process Towards Development of $LiMPO_4$ (M = Fe, Mn) Nanomaterials for Lithium-Ion Batteries. *Adv. Energy Mater.* **2012**, *2*, 284−297.
(24) Wang, L.; He, X. M.; Sun, W. T.; Wang, J. L.; Li, Y. D.; Fan, S. S. Crystal Orientation Tuning of $LiFePO_4$ Nanoplates for High Rate Lithium Battery Cathode Materials. *Nano Lett.* **2012**, *12*, 5632−5636.
(25) Kim, D. H.; Kim, J. Synthesis of $LiFePO_4$ Nanoparticle in Polyol Medium and Their Electrochemical Properties. *Electrochem. Solid-State Lett.* **2006**, *9*, A439−A442.
(26) Kim, D. H.; Im, J. S.; Kang, J. W.; Kim, E. J.; Ahn, H. Y.; Kim, J. A New Synthesis Route to Nanocrystalline Olivine Phosphates and their Electrochemical Properties. *J. Nanosci. Nanotechnol.* **2007**, *7*, 3949−3953.
(27) Jiang, J.; Liu, W.; Chen, J. T.; Hou, Y. L. $LiFePO_4$ Nanocrystals: Liquid-Phase Reduction Synthesis and Their Electrochemical Performance. *ACS Appl. Mater. Interfaces* **2012**, *4*, 3062−3068.
(28) Oh, S. W.; Huang, Z. D.; Zhang, B.; Yu, Y.; He, Y. B.; Kim, J. K. Low Temperature Synthesis of Graphene-Wrapped $LiFePO_4$ Nanorod Cathodes by the Polyol Method. *J. Mater. Chem.* **2012**, *22*, 17215−17221.
(29) Choi, E. S.; Kim, D. H.; Woo, C. H.; Choi, C. H.; Kim, J. Synthesis and Electrochemical Properties of $LiFePO_4$/Carbon Nanocomposites in Polyol Medium. *J. Nanosci. Nanotechnol.* **2010**, *10*, 3416−3419.
(30) Chen, J. J.; Bai, J. M.; Chen, H. Y.; Graetz, J. In Situ Hydrothermal Synthesis of $LiFePO_4$ Studied by Synchrotron X-ray Diffraction. *J. Phys. Chem. Lett.* **2011**, *2*, 1874−1878.
(31) Lee, M. H.; Kim, T. H.; Kim, Y. S.; Park, J. S.; Song, H. K. Optimized Evolution of a Secondary Structure of $LiFePO_4$: Balancing between Shape and Impurities. *J. Mater. Chem.* **2012**, *22*, 8228−8234.
(32) Liu, T. F.; Zhao, L.; Wang, D. L.; Zhu, J. S.; Wang, B.; Guo, C. F. Carbon-Coated Single-Crystalline $LiFePO_4$ Nanocomposites for High-Power Li-Ion Batteries: The Impact of Minimization of the Precursor Particle Size. *RSC Adv.* **2014**, *4*, 10067−10075.
(33) Mori, H.; Ito, T. The Structure of Vivianite and Symplesite. *Acta Crystallogr.* **1950**, *3*, 1−6.
(34) Mattievich, E.; Danon, J. Hydrothermal Synthesis and Mössbauer Studies of Ferrous Phosphate of the Homologous Series $Fe_3^{2+}(PO_4)_2(H_2O)_n$. *J. Inorg. Nucl. Chem.* **1977**, *39*, 569−580.
(35) Francesco, C.; Capitelli, G.; Ghiara, M. R.; Rossi, M. Crystal-Chemical Investigation of $Fe_3(PO_4)_2{\cdot}8H_2O$ Vivianite Minerals. *Z. Kristallogr.* **2012**, *227*, 92−101.
(36) Frost, R. L.; Martens, W.; Williams, P. A.; Kloprogge, J. T. Raman and Infrared Spectroscopic Study of the Vivianite-Group Phosphates Vivianite, Baricite and Bobierrite. *Mineral. Mag.* **2002**, *66*, 1063−1073.
(37) Piriou, B.; Poullen, J. F. Etude Infrarouge des Modes Vibrationnels de L'eau Dans la Vivianite. *Bull. Mineral.* **1987**, *110*, 697−710.
(38) Wang, Y. Q.; Asunskis, D. J.; Sherwood, M. A. Iron II Phosphate $Fe_3(PO_4)_2$ by XPS. *Surf. Sci. Spectra* **2002**, *9*, 91−98.
(39) Grosvenor, A. P.; Kobe, B. A.; Biesinger, M. C.; Mclntyre, N. S. Investigation of Multiplet Splitting of Fe 2p XPS Spectra and Bonding in Iron Compounds. *Surf. Interface Anal.* **2004**, *36*, 1564−1574.
(40) Zhu, J. X.; Fiore, J.; Li, D. S.; Kinsinger, N. M.; Wang, Q. Q.; Masi, E. D.; Guo, J. C.; Kisailus, D. Solvothermal Synthesis, Development, and Performance of $LiFePO_4$ Nanostructures. *Cryst. Growth Des.* **2013**, *13*, 4659−4666.
(41) Chen, J.; Yan, L. M.; Yue, B. H. Nano-Layered $LiFePO_4$ Particles Converted from Nano-Layered Ferrous Phenylphosphonate Templates. *J. Power Sources* **2012**, *209*, 7−14.
(42) Qin, X.; Wang, J. M.; Xie, J.; Li, F. Z.; Wen, L.; Wang, X. H. Hydrothermally Synthesized $LiFePO_4$ Crystals with Enhanced Electrochemical Properties: Simultaneous Suppression of Crystal Growth along [010] and Antisite Defect Formation. *Phys. Chem. Chem. Phys.* **2012**, *14*, 2669−2677.
(43) Chen, C.; Liu, G. B.; Wang, Y.; Li, J. L.; Liu, H. Preparation and Electrochemical Properties of $LiFePO_4$/C Nanocomposite Using $FePO_4{\cdot}2H_2O$ Nanoparticles by Introduction of $Fe_3(PO_4)_2{\cdot}8H_2O$ at Low Cost. *Electrochim. Acta* **2013**, *113*, 464−469.
(44) Zaghib, K.; Guerfi, A.; Hovington, P.; Vijh, A.; Trudeau, M.; Mauger, A.; Goodenough, J. B.; Julien, C. M. Review and Analysis of Nanostructured Olivine-Based Lithium Rechargeable Batteries: Status and Trends. *J. Power Sources* **2013**, *232*, 357−369.

(45) Wang, Y. G.; Wang, Y. R.; Hosono, E. J.; Wang, K. X.; Zhou, H. S. The Design of a $LiFePO_4$/Carbon Nanocomposite with a Core−Shell Structure and Its Synthesis by an In Situ Polymerization Restriction Method. *Angew. Chem., Int. Ed.* **2008**, *47*, 7461−7465.
(46) Ma, Z. P.; Shao, G. J.; Wang, X.; Song, J. J.; Wang, G. L.; Liu, T. T. Solvothermal Synthesis of $LiFePO_4$ Nanoplates with (010) Plane and the Uniform Carbon Coated on Their Surface by Esterification Reaction. *Mater. Chem. Phys.* **2014**, *143*, 969−976.
(47) Wang, J. J.; Sun, X. L. Understanding and Recent Development of Carbon Coating on $LiFePO_4$ Cathode Materials for Lithium-Ion Batteries. *Energy Environ. Sci.* **2012**, *5*, 5163−5185.
(48) Wang, J. J.; Yang, J. L.; Tang, Y. J.; Liu, J.; Zhang, Y.; Liang, G. X.; Gauthier, M.; Chen-Wiegart, Y.-C. K.; Banis, M. N.; Li, X. F.; Li, R.Y.; Wang, J.; Sham, T. K.; Sun, X. L. Size-dependent surface phase change of lithium iron phosphate during carbon coating. *Nat. Commun.* **2014**, *5*, 5.